PHYSICAL REVIEW D **96,** 056008 (2017)

Spacelike and timelike form factors for the $(\pi^0,\eta,\eta')\to\gamma^*\gamma$ transitions in the light-front quark model

Ho-Meoyng Choi
Department of Physics, Teachers College, Kyungpook National University, Daegu 41566, Korea

Hui-Young Ryu
Department of Physics, Pusan National University, Pusan 46241, Korea

Chueng-Ryong Ji
Department of Physics, North Carolina State University, Raleigh, North Carolina 27695-8202, USA
(Received 2 August 2017; published 15 September 2017)

We investigate the $(\pi^0,\eta,\eta')\to\gamma^*\gamma$ transitions both for the spacelike region and the timelike region using the light-front quark model (LFQM). In particular, we present the new direct method to explore the timelike region without resorting to mere analytic continuation from the spacelike region to the timelike region. Our direct calculation in timelike region shows the complete agreement not only with the analytic continuation result from the spacelike region but also with the result from the dispersion relation between the real and imaginary parts of the form factor. For the low energy regime, we compare our LFQM results of the transition form factors (TFFs) for the low timelike momentum transfer region and the slope parameters at $q^2=0$ with the recent experimental data from the Dalitz decays of (π^0,η,η'). For the high energy regime, we incorporate the QCD factorization in our LFQM to examine the asymptotic behavior of TFFs both for the spacelike region and the timelike region. We compare our results with the available experimental data.

DOI: 10.1103/PhysRevD.96.056008

I. INTRODUCTION

The meson-photon transition form factors (TFFs) such as $F_{P\gamma}(Q^2)(P=\pi^0,\eta,\eta')$ have been known to be the simplest exclusive processes involving the strong interaction. They play a significant role in allowing both the low- and high-energy precision tests of the standard model, in particular, the quantum chromodynamics (QCD)[1].

For the low-energy regime, the TFFs enter the prediction of important observables such as the rates of rare decays $P\to\bar{\ell}\ell(\ell=e,\mu)$ [2] and the hadronic light-by-light (HLbL) scattering contribution to the muon anomalous magnetic moment $(g-2)_\mu$ [3,4]. The HLbL contribution is in principle obtained by integrating some weighting functions times the product of a single-virtual and a double-virtual TFFs for spacelike momentum [3,5]. While there are currently no available data for the double-virtual TFFs, the single-virtual TFFs are available from the $\gamma^*\gamma\to(\pi^0,\eta,\eta')$ processes in the small and intermediate momentum transfer range up to $Q^2\sim 8$ GeV^2. The $(\pi^0,\eta,\eta')\to\gamma^*\gamma$ TFFs of the spacelike regon have been measured experimentally by several collaborations [6–8]. Recently, the single-virtual TFFs for small timelike momentum transfer $(q^2=-Q^2>0)$ regions and the slope parameters at $q^2=0$ have also been measured [9–14] from the Dalitz decays $P\to\bar{\ell}\ell\gamma$ where $(2m_\ell)^2\le q^2\le m_P^2$.

For the high-energy regime, the TFFs can be calculated asymptotically at leading twist as a convolution of the perturbative hard scattering amplitude and the gauge-invariant meson distribution amplitude (DA) [15–17] which incorporates the nonperturbative dynamics of QCD bound state. In particular, hadronic DA [15–17] provides an essential information on the QCD interaction of quarks, antiquarks and gluons inside the hadrons and plays an essential role in applying QCD to hard exclusive processes. The prediction for the single-virtual pion TFF, $F_{\pi\gamma}(Q^2)$, at the asymptotic limit $Q^2\to\infty$ is given by the well-known Brodsky-Lepage limit [15]: $Q^2F_{\pi\gamma}(Q^2\to\infty)=\sqrt{2}f_\pi\simeq 0.185\,\text{GeV}$. However, the *BABAR* Collaboration [18] has measured the $F_{\pi\gamma}(Q^2)$ up to about $Q^2\sim 35$ GeV^2 from reaction $e^+e^-\to e^+e^-\pi^0$ in the single tag mode and have shown not only the serious violation of the Brodsky-Lepage limit but also the rapid growth for $Q^2>15$ GeV^2. On the other hand, the subsequent Belle Collaboration [19] has reported their measurement for $F_{\pi\gamma}(Q^2)$ and has shown that the measured values of $Q^2F_{\pi\gamma}(Q^2)$ are consistent with the asymptotic limit of QCD for $Q^2>15$ GeV^2. For the reaction $e^+e^-\to e^+e^-\eta^{(\prime)}$, the subsequent *BABAR* data [20] for the $Q^2F_{\eta^{(\prime)}\gamma}(Q^2)$ TFFs provided a consistency with the perturbative QCD prediction unlike the case of pion TFF [18]. These discrepancies for the results of $Q^2F_{\pi\gamma}(Q^2)$ between the *BABAR* and the Belle data and between $Q^2F_{\pi\gamma}(Q^2)$ and $Q^2F_{\eta^{(\prime)}\gamma}(Q^2)$ TFFs for $Q^2>15$ GeV^2 region have motivated many theoretical studies using various forms of the meson DAs to understand and reconcile those discrepancies [21–53].

To examine the issue of the scaling behavior of $Q^2F_{\pi\gamma}(Q^2)$ in the large Q^2, it may be necessary to analyze the corresponding form factor not only in the spacelike region but also in the timelike region. To explore the timelike region beyond the single Dalitz decays [9–14], the e^+e^- colliders access the values $q^2 > m_P^2$ through the $e^+e^- \to P\gamma$ annihilation processes. Although the data for $F_{\pi\gamma}(q^2)$ in the large timelike q^2 region is not available yet, the *BABAR* Collaboration [54] measured the timelike $F_{\eta^{(\prime)}\gamma}$ TFFs from the reaction $e^+e^- \to \eta^{(\prime)}\gamma$ at an average e^+e^- center of mass energy of $\sqrt{s} = 10.58$ GeV, which corresponds to $q^2 = 112$ GeV^2. However, the theoretical analysis for the timelike region going beyond $q^2 > m_P^2$ is highly nontrivial due to the singular nature and the complexity of the timelike form factor. Some theoretical subtleties regarding on the analytic continuation from the spacelike region to the timelike region can be found in [28,55]. While some theoretical analyses [56,57] for the TFFs in timelike region can also be found for some Dalitz decays ($(2m_\ell)^2 \le q^2 \le m_P^2$), we do not yet find any theoretical analysis going beyond the Dalitz decay region, i.e. $q^2 > m_P^2$ region.

Thus, we attempt to explore the entire timelike region as well as the spacelike region in this work. We extend our previous analysis [58–60] for the single-virtual $P \to \gamma^*\gamma(P = \pi^0, \eta, \eta')$ transition in the spacelike region using the light-front quark model (LFQM) [58–62] to include the entire timelike region. For the low energy regime, we compare our LFQM results of the TFFs for the low timelike momentum transfer region and the slope parameters at $q^2 = 0$ with the recent experimental data from the Dalitz decays of (π^0, η, η') [9–14]. For the high energy regime, we show the asymptotic behavior of TFFs for both space- and timelike regions and compare them with the available experimental data. In particular, we present the new direct method to explore the timelike region without resorting to mere analytic continuation from space- to timelike region. Our direct calculation in timelike region shows the complete agreement with not only the analytic continuation result from spacelike region but also the result from the dispersion relation (DR) between the real and imaginary parts of the form factor.

The paper is organized as follows. In Sec. II, we discuss the meson-photon TFFs in an exactly solvable model first based on the covariant Bethe-Salpeter (BS) model of $(3+1)$-dimensional fermion field theory. It has been a common practice to utilize an exactly solvable manifestly covariant BS model to check the existence (or absence) of the LF zero mode [63–66] as one can pin down the zero mode exactly in the manifestly covariant BS model [67–71]. Performing both manifestly covariant calculation and the LF calculation, we explicitly show the equivalence between the two results and the absence of the zero-mode contribution to the TTF. In the LF calculation, we analyze both $q^+(= q^0 + q^3) \neq 0$ and $q^+ = 0$ frames and show their equivalence in the numerical calculation. We explicitly demonstrate that our direct LFQM result for the timelike form factor is in complete agreement with the result obtained from the DR method. The $\eta - \eta'$ mixing scheme for the calculations of the $(\eta, \eta') \to \gamma^*\gamma$ TFFs is also introduced in this section. In Sec. III, we apply the self-consistent correspondence relations (see, e.g., Eq. (35) in [70]) between the covariant BS model and the LFQM and present the standard LFQM calculation with the more phenomenologically accessible model wave functions provided by the LFQM analysis of meson mass spectra [58,61]. The self-consistent covariant descriptions of the meson TFFs are confirmed in the standard LFQM as we discuss in this section. In Sec. IV, we present our numerical results for the $(\pi^0, \eta, \eta') \to \gamma^*\gamma$ TFFs for both spacelike and timelike regions and compare them with the available experimental data. Summary and discussion follow in Sec. V. In the Appendix, we provide the comparison of the $\eta - \eta'$ mixing angle between the octet-singlet basis and quark-flavor basis.

II. MANIFESTLY COVARIANT MODEL

The transition form factor $F_{P\gamma}$ for the $P \to \gamma^*\gamma$ ($P = \pi^0, \eta, \eta'$) decay is defined from the matrix element of electromagnetic current $\Gamma^\mu = \langle\gamma(P-q)|J^\mu|P(P)\rangle$ as follows:

$$\Gamma^\mu = ie^2F_{P\gamma}(Q^2)\varepsilon^{\mu\nu\rho\sigma}P_\nu\varepsilon_\rho q_\sigma, \tag{1}$$

where P and q are the momenta of the incident pseudoscalar meson and virtual photon, respectively, and ε is the transverse polarization vector of the final (on-shell) photon. This process is illustrated by the Feynman diagram in Fig. 1(a), which represents the amplitude of the virtual photon being attached to the quark line. While we shall only discuss the amplitude shown in Fig. 1(a), the total amplitude should of course include the contribution from the amplitude of the virtual photon being attached to the antiquark line as well as the quark line.

In the exactly solvable manifestly covariant BS model, the covariant amplitude Γ^μ in Fig. 1(a) is obtained by the following momentum integral

$$\Gamma^\mu = ie_Qe_{\bar{Q}}N_c\int\frac{d^4k}{(2\pi)^4}\frac{H_0}{N_{p_1}N_kN_{p_2}}S^\mu, \tag{2}$$

where N_c is the number of colors and $e_{Q(\bar{Q})}$ is the quark (antiquark) electric charge. The denominators $N_{p_j}(= p_j^2 - m_Q^2 + i\varepsilon)(j = 1, 2)$ and $N_k(= k^2 - m_{\bar{Q}}^2 + i\varepsilon)$ come from the intermediate quark and antiquark propagators of mass $m_Q = m_{\bar{Q}}$ carrying the internal four-momenta $p_1 = P - k$, $p_2 = P - q - k$, and k, respectively. The trace term S^μ in Eq. (2) is obtained as

$$\begin{aligned} S^\mu &= \mathrm{Tr}[\Gamma_P(\not{p}_1 + m_Q)\gamma^\mu(\not{p}_2 + m_Q)\not{\varepsilon}(-\not{k} + m_Q)] \\ &= 4im_Q\varepsilon^{\mu\nu\rho\sigma}\{q_\nu\varepsilon_\rho k_\sigma + (P-k)_\nu q_\rho\varepsilon_\sigma\}, \end{aligned} \tag{3}$$

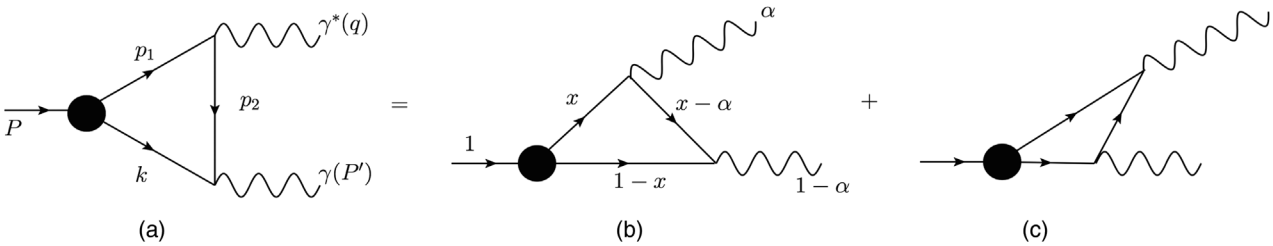

FIG. 1. One-loop Feynman diagrams that contribute to $P \to \gamma^*\gamma$. The single covariant Feynman diagram (a) is the same as the sum of the two LF time-ordered diagrams (b) and (c), respectively.

where we use $\Gamma_P = \gamma_5$ for the pseudoscalar vertex structure. For the $\bar{q}q$ bound-state vertex function $H_0 = H_0(p_1^2, k^2)$ of the meson, we simply take the dimensionless constant parameter g since the covariant loop is regularized with this constant vertex in our model calculation.

Using the following Feynman parametrization for the three propagators

$$\frac{1}{N_{p_1}N_kN_{p_2}} = \int_0^1 dx \int_0^{1-x} dy \times \frac{2}{[N_k + (N_{p_1} - N_k)x + (N_{p_2} - N_k)y]^3}, \quad (4)$$

and shifting the variable k to $k' = k - (x+y)P + yq$, we obtain the manifestly covariant result by defining the amplitude in Fig. 1(a) as $\Gamma^\mu_{(a)} = ie_Q e_{\bar{Q}}[I^{m_Q}_{(a)}]^{\rm Cov}(q^2)\varepsilon^{\mu\nu\rho\sigma}P_\nu\varepsilon_\rho q_\sigma$, where

$$[I^{m_Q}_{(a)}]^{\rm Cov} = \frac{N_c g}{4\pi^2}\int_0^1 dx \int_0^{1-x} dy \times \frac{m_Q}{x(1-x-y)M^2 + xyq^2 - m_Q^2}, \quad (5)$$

with the physical meson mass M. Similarly, the amplitude of the photon being attached to the antiquark line is obtained by changing $x \to 1-x-y$ in Eq. (5) but the two results are found to give the same numerical values. Thus, we obtain the total result as $I^{m_Q}_{\rm tot} = 2[I^{m_Q}_{(a)}]^{\rm Cov}$.

For the LF calculation in parallel with the manifestly covariant one, we use the plus component ($\mu = +$) of the currents J^μ but with two different reference frames, i.e., (1) $q^+ \neq 0$ frame and (2) $q^+ = 0$ frame.

In the $q^+ \neq 0$ frame, we take $P = (P^+, P^-, \mathbf{P}_\perp) = (P^+, M^2/P^+, 0)$ and $q = (q^+, q^-, \mathbf{q}_\perp) = (\alpha P^+, M^2/P^+, 0)$ so that $q^2 = q^+q^-$ of the virtual photon is given by

$$q^2 = \alpha M^2, \quad (6)$$

where $\alpha = q^+/P^+ = 1 - P'^+/P^+$. We should note that $q = (\alpha P^+, M^2/P^+, 0)$ and $P' = P - q = ((1-\alpha)P^+, 0, 0)$ are valid only for $\alpha \neq 1$ but will differ for the $\alpha \to 1$ limit as we shall discuss shortly. In this $q^+ \neq 0$ frame, the Cauchy integration over k^- in Eq. (2) has two nonzero contributions to the residue calculations, i.e., one coming from the interval (i) $0 < k^+ < P'^+$ [see Fig. 1(b)] and the other from (ii) $P'^+ < k^+ < P^+$ [see Fig. 1(c)]. That is, the Feynman covariant diagram in Fig. 1(a) is equivalent to the sum of two LF time-ordered diagrams in Figs. 1(b) and 1(c). The internal momentum k^+ is defined by $k^+ = (1-x)P^+$, where x is the Lorentz invariant longitudinal momentum variable. In this case, the four momenta of the on-mass-shell quark ($p^2_{1\rm on} = m_Q^2$) and antiquark ($k^2_{\rm on} = m_{\bar{Q}}^2$) propagators are defined by $p_{1\rm on} = (xP^+, p^-_{1\rm on}, -\mathbf{k}_\perp)$ and $k_{\rm on} = ((1-x)P^+, k^-_{\rm on}, \mathbf{k}_\perp)$, respectively.

While the residue is at the pole of $k^- = k^-_{\rm on}$, which is placed in the lower half of complex-k^- plane for the region of $0 < k^+ < P'^+$[see Fig. 1(b)], the residue is at the pole of $p_1^- = p^-_{1\rm on}$, which is placed in the upper half of complex-k^- plane for the region of $P'^+ < k^+ < P^+$ [see Fig. 1(c)]. Thus, by defining the amplitude $[\Gamma^+_{(b,c)}]^{\rm LF} \equiv ie_Q e_{\bar{Q}}[I^{m_Q}_{(b,c)}]^{\rm LF}_\alpha(q^2)\varepsilon^{+\nu\rho\sigma}P_\nu\varepsilon_\rho q_\sigma$ for Figs. 1(b) and 1(c), the Cauchy integration of Eq. (2) over k^- in the two regions yields

$$[I^{m_Q}_{(b)}]^{\rm LF}_{0<\alpha<1} = \frac{N_c}{4\pi^3}\int_\alpha^1 \frac{dx}{(1-x)}\int d^2\mathbf{k}_\perp \frac{m_Q}{(\alpha-1)M_0^2}\chi(x,\mathbf{k}_\perp), \quad (7)$$

and

$$[I^{m_Q}_{(c)}]^{\rm LF}_{0<\alpha<1} = \frac{N_c}{4\pi^3}\int_0^\alpha \frac{x'dx}{(1-x)} \times \int d^2\mathbf{k}_\perp \frac{m_Q\chi(x,\mathbf{k}_\perp)}{x'(1-x')M^2 - x(1-x)M_0^2}, \quad (8)$$

respectively, where $x' = x/\alpha$ and

$$\chi(x,\mathbf{k}_\perp) = \frac{g}{x(M^2 - M_0^2)}, \quad (9)$$

with $M_0^2 = \frac{\mathbf{k}_\perp^2 + m_Q^2}{x(1-x)}$ being the invariant mass.[1] We confirmed numerically that $[I^{m_Q}_{(a)}]^{\rm Cov} = [I^{m_Q}_{(b)}]^{\rm LF}_{0<\alpha<1} + [I^{m_Q}_{(c)}]^{\rm LF}_{0<\alpha<1}$ as expected.

[1]For the calculation of the trace term S^μ with $\mu = +$, since the result is given by $S^+ = 8im_Q\varepsilon_{+-xy}P^+(\boldsymbol{\varepsilon}_\perp \times \mathbf{q}_\perp)$, one should first take $\mathbf{q}_\perp \neq 0$ and then take $\mathbf{q}_\perp \to 0$ limit at the end of the trace calculation.

Now, we find a very interesting LF result by taking $\alpha \to 1$ limit, which in fact allows our direct calculation of the timelike TFFs in LFQM possible as we present in the next section, Sec. III. In the $\alpha = 1$ case, the four momenta q and P' are given by $q=(P^+,q^2/P^+,0)$ and $P'=(0,(M^2-q^2)/P^+,0)$, respectively. Since q and P' in the $\alpha = 1$ case are different from the $\alpha \neq 1$ (i.e., $q^2 = \alpha M^2$) case, one should not directly substitute $\alpha = 1$ in Eqs. (7) and (8) to obtain the transition amplitudes corresponding to the $\alpha = 1$ case. To obtain the amplitude for the $\alpha = 1$ case, one needs to go back and start from Eq. (2) again to do the Cauchy integration over k^- with the specifically given four momenta q and P' at $\alpha = 1$. By doing the Cauchy integration of Eq. (2) over k^- in the $\alpha = 1$ case, we find $[I^{m_Q}_{(b)}]^{\rm LF}_{\alpha=1} = 0$ and

$$[I^{m_Q}_{(c)}]^{\rm LF}_{\alpha=1} = \frac{N_c}{4\pi^3}\int_0^1 \frac{dx}{(1-x)^2}\int d^2\mathbf{k}_\perp \frac{m_Q}{M_0^2 - q^2}\chi(x,\mathbf{k}_\perp). \tag{10}$$

That is, we find in the $q^+ \neq 0$ frame at $\alpha = 1$ that only Fig. 1(c) contributes to the total transition amplitude. We also numerically confirm that Eq. (10) exactly coincides with the manifestly covariant result $I^{m_Q}_{(a)}$ given by Eq. (5) as it must be.

For the $q^+ = 0$ frame, we take $P = (P^+, M^2/P^+, 0)$ and $q = (0, q^-, \mathbf{q}_\perp)$ so that $q^2 = -\mathbf{q}_\perp^2 \equiv -Q^2$. Since this $q^+ = 0$ frame essentially corresponds to the $\alpha \to 0$ limit but with $\mathbf{q}_\perp \neq 0$, we refer this frame as the $\alpha = 0$ case in contrast to the $\alpha = 1$ case discussed above. In the $\alpha = 0$ case, we find that only Fig. 1(b) contributes and the Cauchy integration of Eq. (2) over k^- in Fig. 1(b) yields

$$[I^{m_Q}_{(b)}]^{\rm LF}_{\alpha=0} = \frac{N_c}{4\pi^3}\int_0^1 \frac{dx}{x(1-x)}\int d^2\mathbf{k}_\perp \frac{m_Q}{M_0'^2}\chi(x,\mathbf{k}_\perp), \tag{11}$$

where $M_0' = M_0(\mathbf{k}_\perp \to \mathbf{k}'_\perp)$ with $\mathbf{k}'_\perp = \mathbf{k}_\perp + (1-x)\mathbf{q}_\perp$. We again confirmed numerically that Eq. (11) exactly coincides with the manifestly covariant result $I^{m_Q}_{(a)}$ given by Eq. (5) as it must be. Effectively, we obtain $[I^{m_Q}_{(a)}]^{\rm Cov} = [I^{m_Q}_{(c)}]^{\rm LF}_{\alpha=1} = [I^{m_Q}_{(b)}]^{\rm LF}_{\alpha=0} = [I^{m_Q}_{(b)}]^{\rm LF}_{0<\alpha<1} + [I^{m_Q}_{(c)}]^{\rm LF}_{0<\alpha<1}$. This result verifies also the absence of the LF zero-mode in pseudoscalar meson TFFs, i.e., $[I^{m_Q}_{(b)}]^{\rm LF}_{\alpha=1} = 0$ and $[I^{m_Q}_{(c)}]^{\rm LF}_{\alpha=0} = 0$.

For $(\eta,\eta') \to \gamma^*\gamma$ transitions, we take into account the presence of the strange quark and antiquark components in the η and η' mesons as well as their mixing with the nonstrange quark and antiquark components. Making use of the $\eta - \eta'$ mixing scheme (see Appendix), the flavor assignment of η and η' mesons in the quark-flavor basis $\eta_q = (u\bar{u} + d\bar{d})/\sqrt{2}$ and $\eta_s = s\bar{s}$ is given by [72–76]

$$\begin{pmatrix}\eta\\ \eta'\end{pmatrix} = \begin{pmatrix}\cos\phi & -\sin\phi\\ \sin\phi & \cos\phi\end{pmatrix}\begin{pmatrix}\eta_q\\ \eta_s\end{pmatrix}. \tag{12}$$

In this mixing scheme, we obtain the transition form factors $F_{P\gamma}$ for $P \to \gamma^*\gamma(P = \pi^0,\eta,\eta')$ transitions as follows

$$\begin{aligned}
F_{\pi\gamma}(q^2) &= \frac{(e_u^2 - e_d^2)}{\sqrt{2}} I^{m_{u(d)}}_{\rm tot},\\
F_{\eta\gamma}(q^2) &= \cos\phi\frac{(e_u^2 + e_d^2)}{\sqrt{2}} I^{m_{u(d)}}_{\rm tot} - \sin\phi e_s^2 I^{m_s}_{\rm tot},\\
F_{\eta'\gamma}(q^2) &= \sin\phi\frac{(e_u^2 + e_d^2)}{\sqrt{2}} I^{m_{u(d)}}_{\rm tot} + \cos\phi e_s^2 I^{m_s}_{\rm tot},
\end{aligned} \tag{13}$$

where we again should note that $I^{m_Q}_{\rm tot} = 2[I^{m_Q}_{(a)}]^{\rm Cov} = 2([I^{m_Q}_{(b)}]^{\rm LF}_{0<\alpha<1} + [I^{m_Q}_{(c)}]^{\rm LF}_{0<\alpha<1}) = 2[I^{m_Q}_{(c)}]^{\rm LF}_{\alpha=1} = 2[I^{m_Q}_{(b)}]^{\rm LF}_{\alpha=0}$ with the factor 2 needed to include the contribution from the amplitude of the photon attached to the antiquark line.

For the illustration of the numerical results from the exactly solvable BS model calculation, we show the normalized pion TFF $F_{\pi\gamma}(q^2)/F_{\pi\gamma}(0)$ for both space- and timelike regions of momentum transfer $-2 \le q^2 \le 3$ GeV^2 in Fig. 2. The used model parameters are $m_Q = 0.22$ GeV and $M = 0.14$ GeV. We note that the value of g to yield the experimental data value for $F^{\rm Exp}_{\pi\gamma}(0) = 0.272$ GeV^{-1} at $q^2 = 0$ is given by $g = 3.22$. While $F_{\pi\gamma}(q^2)$ in spacelike momentum transfer region ($q^2 < 0$) is real, it becomes complex in timelike region ($q^2 > 0$), $F_{\pi\gamma}(q^2) = {\rm Re}F_{\pi\gamma}(q^2) + i{\rm Im}F_{\pi\gamma}(q^2)$. Figures 2(a) and 2(b) represent the results obtained from $[I^{m_Q}_{(b)}]^{\rm LF}_{0<\alpha<1}$ in Eq. (7) and $[I^{m_Q}_{(c)}]^{\rm LF}_{0<\alpha<1}$ in Eq. (8), respectively. As one can see, the imaginary part ${\rm Im}F_{\pi\gamma}(q^2)$ (red line) of the form factor comes only from Fig. 1(c) and starts to appear from the threshold $q^2 = 4m_Q^2$. Figure 2(c) shows the normalized pion TFF, $F_{\pi\gamma}(q^2)/F_{\pi\gamma}(0)$. The dotted, dashed and solid lines in Fig. 2(c) represent ${\rm Re}[F_{\pi\gamma}(q^2)/F_{\pi\gamma}(0)]$, ${\rm Im}[F_{\pi\gamma}(q^2)/F_{\pi\gamma}(0)]$ and $|F_{\pi\gamma}(q^2)/F_{\pi\gamma}(0)|$, respectively. We confirmed numerically that $[I^{m_Q}_{(a)}]^{\rm Cov} = [I^{m_Q}_{(b)}]^{\rm LF}_{0<\alpha<1} + [I^{m_Q}_{(c)}]^{\rm LF}_{0<\alpha<1} = [I^{m_Q}_{(c)}]^{\rm LF}_{\alpha=1} = [I^{m_Q}_{(b)}]^{\rm LF}_{\alpha=0}$ as mentioned earlier. As a consistency check for our numerical calculations, we also compare our direct results of the form factor $F(q^2) = {\rm Re}F(q^2) + i{\rm Im}F(q^2)$ with those obtained from the dispersion relations (DR) given by

$$\begin{aligned}
{\rm Re}F(q^2) &= \frac{1}{\pi}P\int_{-\infty}^{\infty}\frac{{\rm Im}F(q'^2)}{q'^2 - q^2}dq'^2,\\
{\rm Im}F(q^2) &= -\frac{1}{\pi}P\int_{-\infty}^{\infty}\frac{{\rm Re}F(q'^2)}{q'^2 - q^2}dq'^2,
\end{aligned} \tag{14}$$

where P indicates the Cauchy principal value. In Fig. 2(c), the data denoted by $(\times)$ represents the DR result of

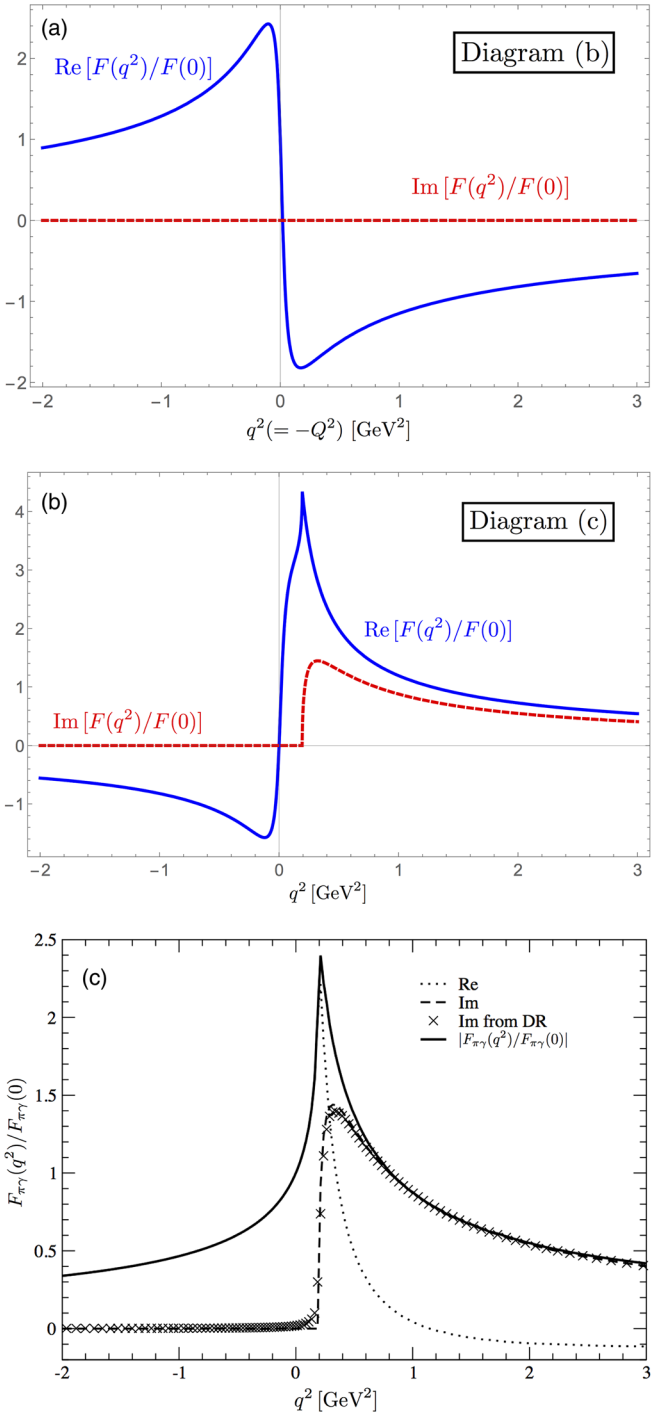

FIG. 2. The exactly solvable BS model calculation of the normalized $F_{\pi\gamma}(q^2)$ for both space- and timelike regions $(-2 \le q^2 \le 3)$ [GeV^2]: (a) and (b) represent the contributions from Figs. 1(b) and 1(c), respectively, for $0 < \alpha < 1$ case. (c) shows the normalized $F_{\pi\gamma}(q^2)/F_{\pi\gamma}(0)$ compared with the dispersion relation.

$\mathrm{Im}F(q^2)$ obtained from Eq. (14) and shows an excellent agreement with our direct result (dashed line). This assures the validity of our numerical calculation in the timelike region.

III. APPLICATION OF THE LIGHT-FRONT QUARK MODEL

In our previous analysis of the twist-2 and twist-3 DAs of pseudoscalar and vector mesons [69–71] and the pion electromagnetic form factor [70], we have shown that standard LF (SLF) results of the LFQM is obtained by the replacement of the LF vertex function χ in the BS model with the Gaussian wave function ϕ_R as follows [see, e.g., Eq. (35) in [70]]

$$\sqrt{2N_c}\frac{\chi(x,\mathbf{k}_\perp)}{1-x} \to \frac{\phi_R(x,\mathbf{k}_\perp)}{\sqrt{\mathbf{k}_\perp^2+m_Q^2}}, \qquad M \to M_0, \tag{15}$$

where $M \to M_0$ implies that the physical mass M included in the integrand of BS amplitude (except M in the vertex function χ) has to be replaced with the invariant mass M_0 since the SLF results of the LFQM are obtained from the requirement of all constituents being on their respective mass-shell. The mapping given by Eq. (15) was originally found for the resolution of the LF zero-mode issue in the vector meson decay constant and its self-consistent covariant description as discussed extensively in [69]. As the mapping however involves only the radial wave function and the meson mass, the same mapping holds for the pseudoscalar mesons as we have discussed in [70,71]. Likewise, the correspondence in Eq. (15) is valid again in this analysis of a $P \to \gamma^*\gamma$ transition.

In the standard LFQM [58,59,61,62,76–79] approach, the wave function of a ground state pseudoscalar meson as a $q\bar{q}$ bound state is given by

$$\Psi_{\lambda\bar{\lambda}}(x,\mathbf{k}_\perp) = \phi_R(x,\mathbf{k}_\perp)\mathcal{R}_{\lambda\bar{\lambda}}(x,\mathbf{k}_\perp), \tag{16}$$

where ϕ_R is the radial wave function and the spin-orbit wave function $\mathcal{R}_{\lambda\bar{\lambda}}$ with the helicity $\lambda(\bar{\lambda})$ of a quark (antiquark) is obtained by the interaction-independent Melosh transformation [80] from the ordinary spin-orbit wave function assigned by the quantum numbers J^{PC}.

For the equal quark and antiquark mass $m_Q = m_{\bar{Q}}$, the Gaussian wave function ϕ_R is given by

$$\phi_R(x,\mathbf{k}_\perp) = \frac{4\pi^{3/4}}{\beta^{3/2}}\sqrt{\frac{M_0}{4x(1-x)}}e^{m_Q^2/2\beta^2}e^{-M_0^2/8\beta^2}, \tag{17}$$

where $\partial k_z/\partial x = M_0/4x(1-x)$ is the Jacobian of the variable transformation $\{x,\mathbf{k}_\perp\} \to \vec{k} = (\mathbf{k}_\perp, k_z)$ and β is the variational parameter fixed by our previous analysis of meson mass spectra [58,61,62]. The covariant form of the spin-orbit wave function $\mathcal{R}_{\lambda\bar{\lambda}}$ is given by

$$\mathcal{R}_{\lambda\bar{\lambda}} = \frac{\bar{u}_\lambda(p_Q)\gamma_5 v_{\bar{\lambda}}(p_{\bar{Q}})}{\sqrt{2}M_0}, \tag{18}$$

and it satisfies $\sum_{\lambda\bar{\lambda}}\mathcal{R}^{\dagger}_{\lambda\bar{\lambda}}\mathcal{R}_{\lambda\bar{\lambda}}=1$. Thus, the normalization of our wave function is given by

$$1=\int_0^1 dx\int\frac{d^2\mathbf{k}_\perp}{16\pi^3}|\phi_R(x,\mathbf{k}_\perp)|^2. \tag{19}$$

Applying the correspondence given by Eq. (15) to $[I^{m_Q}_{(c)}]^{\rm LF}_{\alpha=1}$ in Eq. (10) and $[I^{m_Q}_{(b)}]^{\rm LF}_{\alpha=0}$ in Eq. (11), we obtain the corresponding SLF results $[I^{m_Q}_{\rm tot}]^{\rm SLF}_{\alpha=1}$ and $[I^{m_Q}_{\rm tot}]^{\rm SLF}_{\alpha=0}$ in our LFQM as follows:

$$[I^{m_Q}_{\rm tot}]^{\rm SLF}_{\alpha=1}=\frac{\sqrt{2N_c}}{4\pi^3}\int_0^1\frac{dx}{(1-x)}\int d^2\mathbf{k}_\perp \times\frac{m_Q}{M_0^2-q^2}\frac{\phi_R(x,\mathbf{k}_\perp)}{\sqrt{\mathbf{k}_\perp^2+m_Q^2}}, \tag{20}$$

and

$$[I^{m_Q}_{\rm tot}]^{\rm SLF}_{\alpha=0}=\frac{\sqrt{2N_c}}{4\pi^3}\int_0^1\frac{dx}{x}\int d^2\mathbf{k}_\perp\frac{m_Q}{M_0'^2}\frac{\phi_R(x,\mathbf{k}_\perp)}{\sqrt{\mathbf{k}_\perp^2+m_Q^2}}, \tag{21}$$

respectively. We confirm that our result is frame-independent, i.e., $[I^{m_Q}_{\rm tot}]^{\rm SLF}_{0<\alpha<1}=[I^{m_Q}_{\rm tot}]^{\rm SLF}_{\alpha=1}=[I^{m_Q}_{\rm tot}]^{\rm SLF}_{\alpha=0}$. While the TFFs for $P\to\gamma^*\gamma$ can be obtained by substituting either $[I^{m_Q}_{\rm tot}]^{\rm SLF}_{\alpha=1}$ or $[I^{m_Q}_{\rm tot}]^{\rm SLF}_{\alpha=0}$ into Eq. (13), we shall use $[I^{m_Q}_{\rm tot}]^{\rm SLF}_{\alpha=1}$ for the analysis of the timelike region due to the simple and clean pole structure given by $(M_0^2-q^2)^{-1}$ in Eq. (20) compared to the pole appearing through $[M_0'^2]^{-1}$ in Eq. (21). It is important to notice that the internal transverse momentum $\mathbf{k}_\perp$ does not mix with the external virtual photon momentum $q=(P^+,q^2/P^+,0)$ in $\alpha=1$ case as shown in Eq. (20) so that the direct timelike TFF calculation can be done most effectively. For sufficiently high spacelike momentum transfer $Q^2(=-q^2=\mathbf{q}_\perp^2)$ region, both Eqs. (20) and (21) can be approximated in the leading order of $1/Q^2$ as follows

$$[I^{m_Q}_{\rm tot}]^{\rm SLF}\simeq 2f_P\int_0^1\frac{dx}{(1-x)Q^2}\int d^2\mathbf{k}_\perp\psi_P(x,\mathbf{k}), \tag{22}$$

where f_P is the pseudoscalar meson decay constant and $\psi_P(x,\mathbf{k}_\perp)$ is the transverse momentum dependent DA (TMDA) [81] that is a 3-dimensional generalization of the twist-2 pseudoscalar meson DA $\phi_{2;P}(x)$:

$$\phi_{2;P}(x)=\frac{\sqrt{2N_c}}{f_P 8\pi^3}\int d^2\mathbf{k}_\perp\frac{\phi_R(x,\mathbf{k}_\perp)}{\sqrt{\mathbf{k}_\perp^2+m_Q^2}}m_Q =\int_0^\infty d^2\mathbf{k}_\perp\psi_P(x,\mathbf{k}_\perp). \tag{23}$$

From Eqs. (13), (22) and (23), one can verify that our LFQM result for $F_{\pi\gamma}(Q^2)$ at sufficiently high Q^2 can be approximated as

$$F_{\pi\gamma}(Q^2)\simeq\frac{\sqrt{2}f_\pi}{3}\int_0^1\frac{dx}{(1-x)Q^2}\phi_{2;\pi}(x). \tag{24}$$

The asymptotic PQCD DA, $\phi_{2;\pi}(x)=6x(1-x)$, leads to the well-known Brodsky-Lepage limit [15]: $Q^2F_{\pi\gamma}(Q^2\to\infty)=\sqrt{2}f_\pi\simeq 0.185\,\text{GeV}$.

Applying our LFQM to calculate the decay widths for $P\to\gamma\gamma(P=\pi^0,\eta,\eta')$ transition, the decay width for $P\to\gamma\gamma$ is given by

$$\Gamma_{P\to\gamma\gamma}=\frac{\pi}{4}\alpha^2M^3|F_{P\gamma}(0)|^2, \tag{25}$$

where α is the fine structure constant. The form factor $F_{P\gamma}(0)$ at $Q^2=0$ may also be expressed in terms of the decay constants obtained from the Adler-Bell-Jackiw (ABJ) anomaly (or the chiral anomaly) [82,83] as follows

$$F^{\rm ABJ}_{\pi\gamma}(0)=\frac{1}{2\sqrt{2}\pi^2f_\pi},$$
$$F^{\rm ABJ}_{\eta\gamma}(0)=\frac{1}{2\sqrt{6}\pi^2}\left[\frac{1}{f_8}\cos\theta-\frac{2\sqrt{2}}{f_0}\sin\theta\right],$$
$$F^{\rm ABJ}_{\eta'\gamma}(0)=\frac{1}{2\sqrt{6}\pi^2}\left[\frac{1}{f_8}\sin\theta+\frac{2\sqrt{2}}{f_0}\cos\theta\right], \tag{26}$$

where θ is the mixing angle in the flavor SU(3) octet-singlet basis and is related with the mixing angle ϕ in the quark-flavor basis via $\theta=\phi-\arctan\sqrt{2}\simeq\phi-54.7°$. While the quadratic (linear) Gell-Mann-Okubo mass formula prefers $\theta\simeq-10°$, $\phi\simeq 44.7°$ ($\theta\simeq-23°$, $\phi\simeq 31.7°$), the KLOE Collaboration [84] extracted the pseudoscalar mixing angle ϕ by measuring the ratio $\text{BR}(\phi\to\eta'\gamma)/\text{BR}(\phi\to\eta\gamma)$. The measured values are $\phi=(39.7\pm0.7)°$ and $(41.5\pm0.3_{\rm stat}\pm0.7_{\rm syst}\pm0.6_{\rm th})°$ with and without the gluonium content for η', respectively. The mixing angle has also been analyzed on lattice by the RBC-UKQCD Collaboration [85], where $\theta=-14.1(2.8)°$ was obtained. However, since the mixing angle for $\eta-\eta'$ is still a controversial issue, we use more conservatively $\phi=37°\pm5°$ to check the sensitivity of our LFQM.

IV. NUMERICAL RESULTS

In our numerical calculations within the standard LFQM, we use the model parameters (i.e. constituent quark masses m_Q and the gaussian parameters $\beta_{Q\bar{Q}}$) for the linear confining potentials given in Table I, which were obtained from the calculation of meson mass spectra using the variational principle in our LFQM [58,59,61]. For the model parameters given in Table I, our LFQM predictions of the decay constants for the pion, octet (η_8) and singlet (η_0) mesons are $f_\pi=130$ MeV, $f_8/f_\pi=1.32$, and $f_0/f_\pi=1.16$, respectively. Our results of the octet and singlet meson decay constants are quite comparable with

TABLE I. The constituent quark masses $m_Q(Q = u(d), s)$ (in GeV) and the Gaussian parameters $\beta_{Q\bar{Q}}$ (in GeV) for the linear confining potentials obtained from the variational principle in our LFQM [58,59,61].

$m_{u(d)}$	m_s	$\beta_{Q\bar{Q}}$	$\beta_{s\bar{s}}$
0.22	0.45	0.3659	0.4128

TABLE II. Form factor $F_{P\gamma}(0)$ (in GeV^{-1}) for $(P = \pi^0, \eta, \eta') \to \gamma\gamma$.

Model	$F_{P\gamma}^{\mathrm{Th}}(0)$	$F_{P\gamma}^{\mathrm{ABJ}}(0)$	$F_{P\gamma}^{\mathrm{Exp}}(0)$
$\pi \to \gamma\gamma$	0.242	0.276	0.272(3)
$\eta \to \gamma\gamma$ (for $\phi = 37^{-5^\circ}_{+5}$)	$0.286^{+0.024}_{-0.027}$	$0.232^{+0.029}_{-0.030}$	0.274(5)
$\eta' \to \gamma\gamma$ (for $\phi = 37^{-5^\circ}_{+5}$)	$0.290^{-0.026}_{+0.024}$	$0.332^{-0.021}_{+0.025}$	0.344(6)

other theoretical predictions such as $f_8/f_\pi = 1.26$ and $f_0/f_\pi = 1.17$ [72], $f_8/f_\pi = 1.28$ and $f_0/f_\pi = 1.25$ [74], and $f_8/f_\pi = 1.25$ and $f_0/f_\pi = 1.04 \pm 0.04$ [86].

For the numerical computations of the TFFs given by Eq. (13) using our LFQM, we use the result $[I_{\mathrm{tot}}^{m_Q}]_{\alpha=1}^{\mathrm{SLF}}$ in Eq. (20) since it is much more convenient to handle the singularities in timelike momentum transfer region than any other reference frame. In Table II, we summarize our LFQM results of form factor $F_{P\gamma}(0)$ for $(P = \pi^0, \eta, \eta') \to \gamma\gamma$ obtained from the direct calculation $[F_{P\gamma}^{\mathrm{Th}}(0)]$ (see Eqs. (13) and (20)) and from the ABJ formulas $[F_{P\gamma}^{\mathrm{ABJ}}(0)]$ [see Eq. (26)] compared with the experimental data [87,88]. For the $(\eta, \eta') \to \gamma\gamma$ processes, we use the mixing angles $\phi = 37^{-5^\circ}_{+5}$ in the quark-flavor basis. The experimental values of $F_{\eta\gamma}^{\mathrm{Exp}}(0) = 0.274(5)\ \mathrm{GeV}^{-1}$ and $F_{\eta'\gamma}^{\mathrm{Exp}}(0) = 0.344(6)\ \mathrm{GeV}^{-1}$ were extracted from the measured decay widths $\Gamma^{\mathrm{Exp}}(\eta \to \gamma\gamma) = 0.516(18)$ keV (obtained after combining the PDG average [87] together with the recent KLOE-2 result [88]) and $\Gamma^{\mathrm{Exp}}(\eta' \to \gamma\gamma) = 4.35(14)$ keV, respectively. For the $\pi^0 \to \gamma\gamma$ case, while our result $F_{\pi\gamma}^{\mathrm{ABJ}}(0) = 0.276\ \mathrm{GeV}^{-1}$ obtained from ABJ anomaly is in good agreement with the data, the direct result $F_{\pi\gamma}^{\mathrm{Th}}(0) = 0.242\ \mathrm{GeV}^{-1}$ accounts for about 90% of the data. For the $(\eta, \eta') \to \gamma\gamma$ case, while our results $F_{P\gamma}^{\mathrm{ABJ}}(0)$ prefer $\phi \simeq 32^\circ$ to fit the data, the direct results $F_{P\gamma}^{\mathrm{Th}}(0)$ prefer $\phi \simeq 40^\circ$ for the best fits of both η and η' TFFs.

From the point of view of QCD, the twist-2 DA $\phi_{2;P}(x)$ of a hadron depends on the scale μ which separates nonperturbative and perturbative regimes. In our LFQM, we can associate μ with the transverse integration cutoff via $|\mathbf{k}_\perp| \le \mu$, which is the usual way how the normalization scale is defined for the LF wave function (see, e.g. Ref. [15]). In order to estimate this cutoff value, we made a three-dimensional plot for TMDA $\psi_P(x, \mathbf{k}_\perp)$ in Eq. (23) in the form of $\psi_P(x, y)$ by changing the variable $\mathbf{k}_\perp^2 = y/(1-y)$ so that

$$\phi_{2;P}(x) = \int_0^\infty d^2\mathbf{k}_\perp \psi_P(x, \mathbf{k}_\perp) = \int_0^1 dy \psi_P(x, y), \qquad (27)$$

where $\psi_P(x, y) = \pi\psi_P(x, |\mathbf{k}_\perp| = \sqrt{y/(1-y)})/(1-y)^2$.

Figure 3 shows the three-dimensional plot (left panel) of $\psi_\pi(x, y)$ for the pion and the corresponding two-dimensional contour plot (right panel). In fact, we obtain the twist-2 pion DA $\phi_{2;\pi}(x)$ by performing the transverse integration up to infinity (or equivalently y up to 1) without

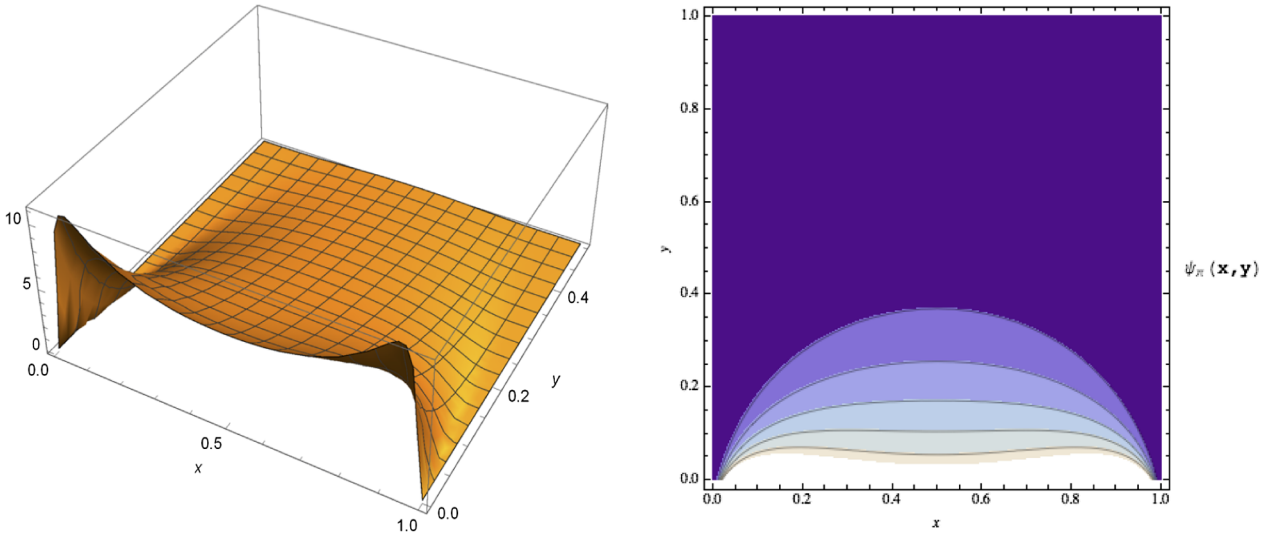

FIG. 3. Transverse momentum dependent distribution amplitude (TMDA) $\psi_\pi(x, \mathbf{k}_\perp)$ (left panel) for the pion in the form of $\psi_\pi(x, y)$ [see Eq. (27)] and the corresponding two-dimensional contour plot (right panel).

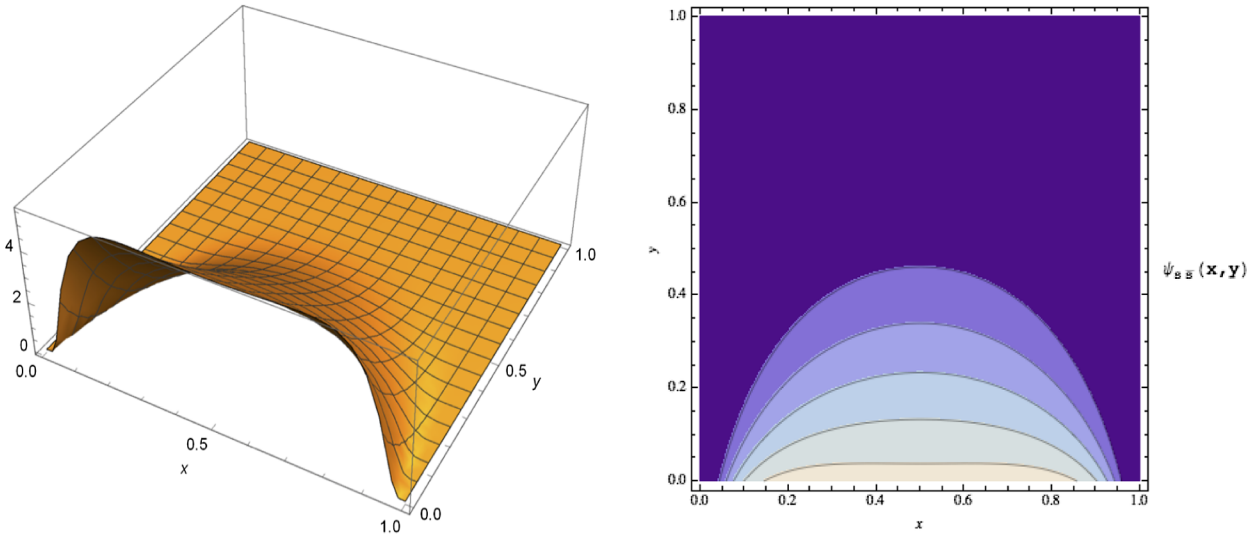

FIG. 4. Transverse momentum dependent distribution amplitude (TMDA) $\psi_{s\bar{s}}(x, \mathbf{k}_\perp)$ (left panel) for the $s\bar{s}$ sector in the form of $\psi_{s\bar{s}}(x, y)$ [see Eq. (27)] and the corresponding two-dimensional contour plot (right panel).

loss of accuracy due to the presence of Gaussian damping factor. However, we find that the integration up to $y \simeq 0.5$ (or equivalently $\mu \simeq |\mathbf{k}_\perp| \simeq 1$ GeV) of $\psi_\pi(x, y)$ makes up 99% of the full result for $\phi_{2;\pi}(x)$. This implies that our cutoff scale corresponds to $\mu \simeq |\mathbf{k}_\perp| \simeq 1$ GeV for the calculation of the twist-2 $\phi_{2;\pi}(x)$. The twist-2 and twist-3 DAs for π can be found in our previous works [59,70,71]. In Fig. 4, we show the three-dimensional plot (left panel) of $\psi_{s\bar{s}}(x, y)$ for the $s\bar{s}$ sector and the corresponding two-dimensional contour plot (right panel). In the case of $s\bar{s}$ sector, the cutoff scale corresponds to $\mu \simeq 1.13$ GeV.

In Fig. 5, we show the normalized $\pi^0 \to \gamma^*\gamma$ TFF $F_{\pi\gamma}(Q^2)/F_{\pi\gamma}(0)$ [see Fig. 5(a)] and $|Q^2 F_{\pi\gamma}(Q^2)|$ [see Fig. 5(b)] for both timelike ($q^2 = -Q^2 > 0$) and spacelike ($q^2 = -Q^2 < 0$) momentum transfer region using Eqs. (13) and (20) and compare them with the available experimental data for the spacelike region [6,7,18,19] and for the small timelike region ($0 < q^2 < m_\pi^2$ GeV^2) obtained from the pion Dalitz decay [13]. The dotted, dashed and solid lines in Fig. 5(a) represent our LFQM predictions of $\mathrm{Re}[F_{\pi\gamma}(q^2)/F_{\pi\gamma}(0)]$, $\mathrm{Im}[F_{\pi\gamma}(q^2)/F_{\pi\gamma}(0)]$ and $|F_{\pi\gamma}(q^2)/F_{\pi\gamma}(0)|$, respectively. We note that the spacelike region can be easily obtained by analytically continuing the momentum transfer $q^2 \to -q^2$ in the integrand of Eq. (20). As one can see from Fig. 5, our result for low- and intermediate- spacelike Q^2 region show a good agreement with the data.

As a consistency check of our LFQM calculations for the timelike region, we also include the real (imaginary) part of the form factor obtained from the DR (denoted by $+(\times)$ data points) given by Eq. (14). As one can see, our direct results for the real and imaginary parts are in perfect agreement with the results obtained from the DR. While the exactly solvable BS model calculation shows the dominant contribution of $\mathrm{Im}F_{\pi\gamma}$ for most of the timelike region, the LFQM result of $\mathrm{Im}F_{\pi\gamma}$ with the more realistic Gaussian radial wave function shows dominant contribution only near the resonance region and the timelike region above $q^2 > 1$ GeV^2 is dominated by the real part contribution. That is, the relative contribution between the real and imaginary parts depends on the shape of the hadron bound state wave function. We also note that Kroll [28] made a rough estimate for the expected size of the timelike form factor using the modified perturbative approach (MPA) [89,90], i.e., the timelike form factor is dominantly real for q^2 larger than 5 GeV^2, its imaginary part contributes less than about 10% to the absolute value. Kroll's discussion about the relative strength between the real and imaginary parts is qualitatively consistent with our LFQM prediction and the reason for this may be attributed to the usage of similar type of the Gaussian wave function.

As one can see from Fig. 5(a), our result for the small timelike region is in good agreement with the very recent measurement of the $\pi^0 \to e^+e^-\gamma$ Dalitz decay from the A2 Collaboration [13]. The slope parameter can be defined from the vector meson dominance (VMD) model in which the normalized TFF is typically parametrized as [87]

$$F_P(m_{ll}) = \frac{1}{1 - \frac{m_{ll}^2}{\Lambda_P^2}} \simeq 1 + a_P \frac{m_{ll}^2}{m_P^2}, \tag{28}$$

where $m_{ll} = \sqrt{q^2}$ is the dilepton invariant mass and $a_P = (m_P/\Lambda_P)^2$ reflects the form-factor slope at $q^2 = 0$. Our result for the slope parameter a_π for the π^0 TFF is obtained as

$$a_\pi = 0.0355, \tag{29}$$

which shows a good agreement with the current world average $a_\pi = 0.032 \pm 0.004$ [87] obtained from timelike measurements [91–93] and the extrapolation of spacelike

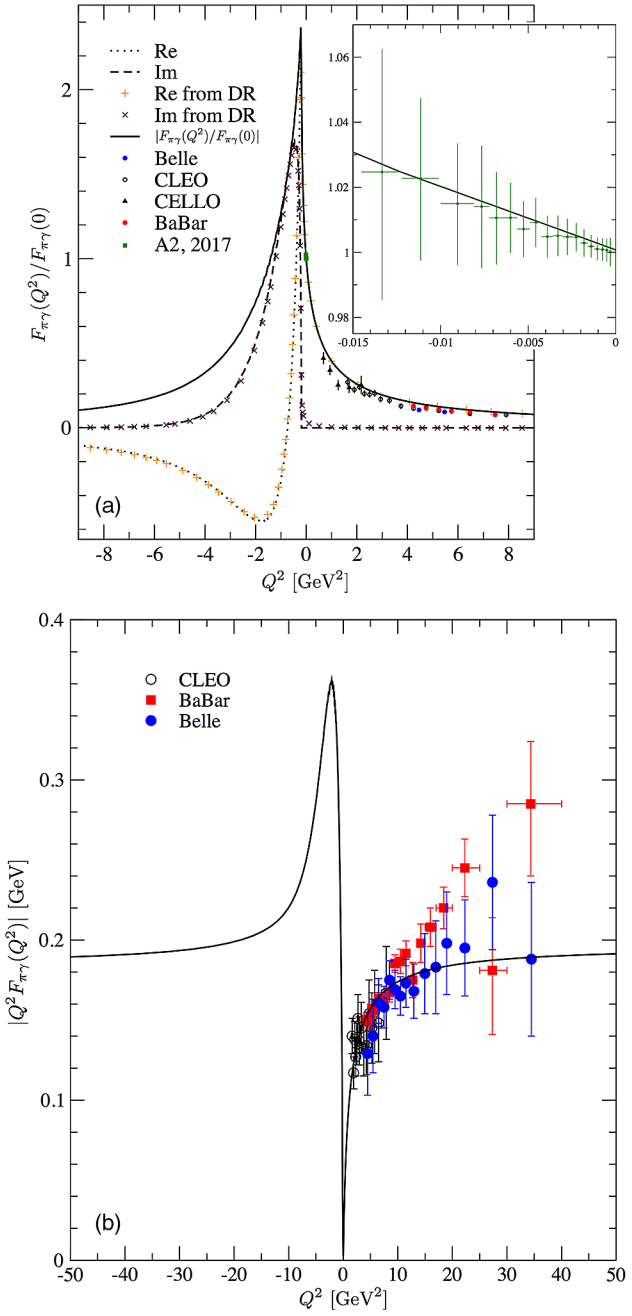

FIG. 5. (a) The the normalized $\pi \to \gamma^*\gamma$ transition form factor $F_{\pi\gamma}(Q^2)/F_{\pi\gamma}(0)$, and (b) $|Q^2F_{\pi\gamma}(Q^2)|$ for both timelike ($q^2 = -Q^2 > 0$) and spacelike ($q^2 = -Q^2 < 0$) momentum transfer regions. The data are taken from [6,7,13,18,19] and [13].

data [6] using a VMD model, as well as the two recent experimental data extracted from the $\pi^0 \to e^+e^-\gamma$ Dalitz decay, $a_\pi = 0.030 \pm 0.010$ from A2 Collaboration [13] and $a_\pi = 0.0368 \pm 0.0057$ from NA62 Collaboration [10]. Our result should also be compared with other theoretical predictions: $a_\pi = 0.0288(42)$ from a Lattice QCD with two flavors of quarks [5]; $a_\pi = 0.0324(12)_{\rm stat}(19)_{\rm syst}$ from the method of Padé approximants [94]; $a_\pi = 0.032(1)$ from a Regge analysis [95]; $a_\pi = 0.036$ from the ChPT [96]; $a_\pi = 0.029(5)$ from a study of the Dalitz decay of π^0 [97]; $a_\pi \approx 0.031$ [98] and $a_\pi \approx 0.035$ [99] from a hard-wall holographic model of QCD; and $a_\pi = 0.024(5)$ [100] from a soft-wall holographic model of QCD. For the analysis of timelike form factor near resonance region in Fig. 5(a), the maximum value of $F_{\pi\gamma}(q^2)$ occurs at $q^2 \simeq 4m_Q^2$ due to the virtual photon wave function term $1/(M_0^2 - q^2)$ in Eq. (20). Since the peak position of the timelike TFF in our LFQM depends on the value of the constituent quark mass, the ρ-pole type resonance may be obtained by simply taking $m_{u(d)} = M_\rho/2$.

Figure 5(b) shows $|Q^2F_{\pi\gamma}(Q^2)|$ for the extensive range ($-50 \le Q^2 \le 50$ GeV^2) of both time- and spacelike momentum transfer regions compared with the spacelike experimental data [7,18,19]. We note that our LFQM result for $|Q^2F_{\pi\gamma}(Q^2)|$ for the spacelike region $10 \le Q^2 \le 45$ GeV^2 is in good agreement with the data from Belle [19] showing the asymptotic behavior but disagree with the *BABAR* data [18] showing the rapid growth for this Q^2 regime. In our LFQM calculation for the perturbative region, we find slightly different values for the timelike and spacelike TFFs, e.g. we find the absolute values of $|Q^2F_{\pi\gamma}(Q^2)| \simeq 0.194$ GeV in the spacelike region and $|q^2F_{\pi\gamma}(q^2)| \simeq 0.186$ GeV in the timelike region at $|Q^2| = 112$ GeV^2, respectively. Although there may be some contributions from the higher-twist and higher Fock-state as discussed in [32], however, we infer from the results shown in Fig. 5 that the higher Fock-state contribution may not be large, especially, for high Q^2 regime.

In Fig. 6, we show the normalized $\eta \to \gamma^*\gamma$ TFF $|F_{\eta\gamma}(Q^2)/F_{\eta\gamma}(0)|$ [see Fig. 6(a)] and $|Q^2F_{\eta\gamma}(Q^2)|$ [see Fig. 6(b)] for both time- and spacelike momentum transfer region. The corresponding figures for η' TFFs are shown in Fig. 7. Since the patterns for the real and imaginary parts of the η and η' TFFs are similar to those of π^0 TFF, we only show the total results for the η and η' TFFs but varying the mixing angles. Since they are rather sensitive to the $\eta - \eta'$ mixing angles, we display the results with the variation of the mixing angles as a sensitivity check. The dot-dashed, solid, and dashed lines for $|F_{\eta\gamma}(q^2)/F_{\eta\gamma}(0)|$ in Fig. 6 and $|F_{\eta'\gamma}(q^2)/F_{\eta'\gamma}(0)|$ in Fig. 7 are obtained from the mixing angles with $\phi_{\eta-\eta'} = 32°$, 37° and 42°, respectively. The experimental data for spacelike region are taken from [6,7,20]. The small timelike data in Figs. 6(a) and 7(a) are taken from the measurements of the η ($0 \le q^2 \le M_\eta^2$ GeV^2) and η' ($0 \le q^2 \le M_{\eta'}^2$ GeV^2) Dalitz decays; $\eta \to \ell\bar{\ell}\gamma(\ell = e, \mu)$ [9,11,12] and $\eta' \to e^+e^-\gamma$ [14].

For the small and medium momentum transfer in both timelike and spacelike region (i.e. $-8 \le Q^2 \le 8$ GeV^2) as shown in Figs. 6(a) and 7(a), both normalized TFFs $F_{\eta\gamma}$ and $F_{\eta'\gamma}$ are not sensitive to the variation of the mixing angles $\phi_{\eta-\eta'} = (37 \pm 5)°$ and show good agreement with the available data in spacelike region [6,7,20]. For the comparison with the timelike data from the (η, η') Dalitz

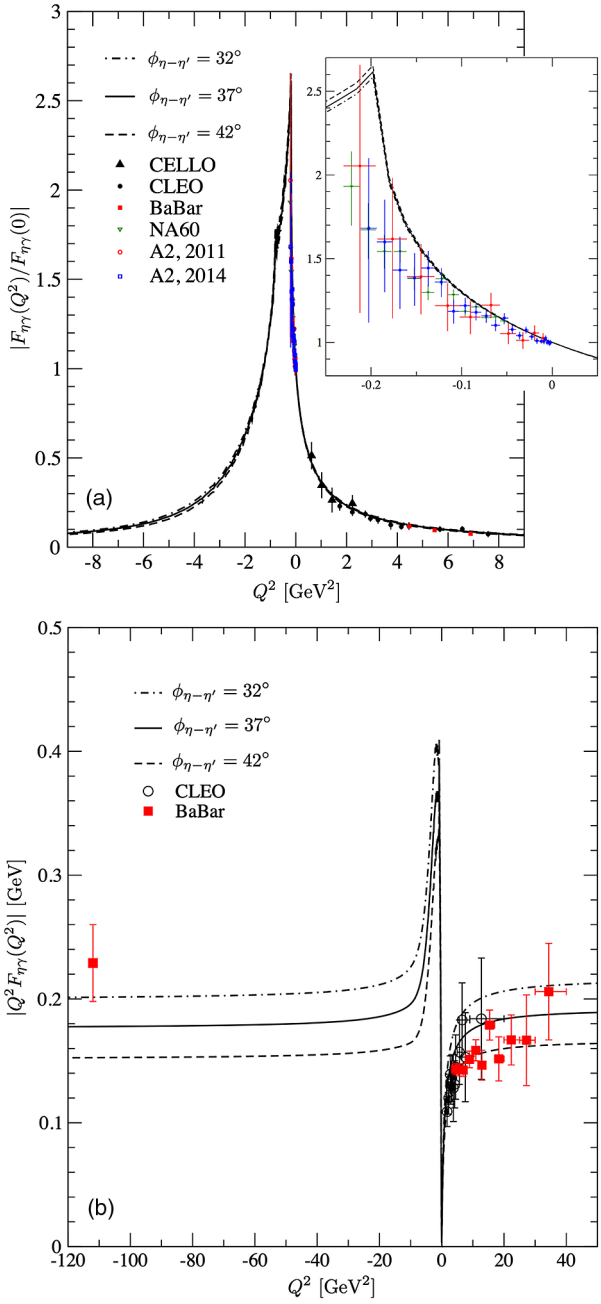

FIG. 6. (a) The normalized $\eta \to \gamma^*\gamma$ transition form factor $|F_{\eta\gamma}(Q^2)/F_{\eta\gamma}(0)|$, and (b) $|Q^2F_{\eta\gamma}(Q^2)|$ for both timelike ($q^2 = -Q^2 > 0$) and spacelike ($q^2 = -Q^2 < 0$) momentum transfer region. The dot-dashed, solid, and dashed lines are results obtained from the mixing angles with $\phi_{\eta-\eta'} = 32°$, 37° and 42°, respectively, and the data are taken from [6,7,9,11,12,20].

decays, we obtain the slope parameters $\Lambda^{-2}_{\eta(\eta')} = a_{\eta(\eta')}/m^2_{\eta(\eta')}$ defined by Eq. (28) as follows

$$\Lambda_\eta^{-2} = 2.112^{-0.031}_{+0.038}\ \text{GeV}^{-2} \quad \text{for } \phi = 37^{-5^\circ}_{+5^\circ},$$
$$\Lambda_{\eta'}^{-2} = 1.732^{-0.035}_{+0.031}\ \text{GeV}^{-2} \quad \text{for } \phi = 37^{-5^\circ}_{+5^\circ}, \tag{30}$$

which correspond to $\Lambda_\eta = 688^{+5}_{-6}$ MeV and $\Lambda_{\eta'} = 760^{+8}_{-7}$ MeV for $\phi = 37^{-5^\circ}_{+5^\circ}$, respectively. Our results for the slope parameters for η and η' TFFs are consistent with the available experimental data within the error bars: $\Lambda_\eta^{-2} = (1.95 \pm 0.22)$ GeV^{-2} [9] and (1.95 ± 0.25) GeV^{-2} [11] for η TFF, and $\Lambda_{\eta'}^{-2} = (1.60 \pm 0.16)$ GeV^{-2} [6], (1.6 ± 0.25) GeV^{-2} [14], and (1.7 ± 0.4) GeV^{-2} [101] for η' TFF, respectively. We also should note that the ratio of $\Lambda_{\eta'}$ to Λ_η is insensitive to the mixing angle, i.e., $\Lambda_{\eta'}/\Lambda_\eta \simeq 1.11$ for $32° \le \phi \le 42°$.

For the resonance properties of $F_{\eta\gamma}$ and $F_{\eta'\gamma}$ within our LFQM as shown in Figs. 6(a) and 7(a), the primary and secondary peaks of both $F_{\eta\gamma}(q^2)$ and $F_{\eta'\gamma}(q^2)$ occurs at $q^2 \simeq 4m_Q^2 (Q = u, d)$ and $q^2 \simeq 4m_s^2$, respectively, regardless of their mixing angles. That is, the $\eta - \eta'$ mixing effect is not significant for the small timelike region corresponding to the η- and η'- Dalitz decays. Particularly, the secondary peak for $F_{\eta'\gamma}$ is more pronounced than that for $F_{\eta\gamma}$. This may be ascribed to the fact that $F_{\eta'\gamma}$ receives contribution more from $s\bar{s}$ component than $Q\bar{Q}(Q = u, d)$ components. For this kinematic regions of the η- and η' Dalitz decays, while our LFQM result for the $F_{\eta\gamma}$ is quite comparable with the data [9,11,12], our result for $F_{\eta'\gamma}$ shows large deviation from the recent BESIII data [14] except near $q^2 = 0$ region. This large deviation for $F_{\eta'\gamma}$ near $q^2 = M_\rho^2$ may be expected from the property of our LFQM, in which the primary peak appears at $q^2 = 4m^2_{u(d)}$ rather than $q^2 = M_\rho^2$. We expect from our LFQM analysis that the experimental data for both timelike $F_{\eta\gamma}$ and $F_{\eta'\gamma}$ would show peaks near $q^2 = M_\rho^2$ and $q^2 = M_\phi^2$ corresponding to our primary and secondary peaks at $q^2 = 4m^2_{u(d)}$ and $q^2 = m_s^2$, respectively.

While the mixing angle effects on $F_{\eta\gamma}$ and $F_{\eta'\gamma}$ do not appear too significant for small and medium momentum transfer region (i.e. $|Q^2| < 8$ GeV^2) as shown in Figs. 6(a) and 7(a), its effects become substantial for large momentum transfer region (i.e., $|Q^2| > 10$ GeV^2) as shown in Figs. 6(b) and 7(b). As in the case of $\pi^0 \to \gamma^*\gamma$ transition, our predictions for both $|Q^2F_{\eta\gamma}(Q^2)|$ and $|Q^2F_{\eta'\gamma}(Q^2)|$ show asymptotic behavior for $|Q^2| \ge 40$ GeV^2 region. The single timelike data at $q^2 = s = 112$ GeV^2 in Fig. 6(b) and the one in Fig. 7(b) are taken from the measurement of $e^+e^- \to \gamma^* \to \eta(\eta')\gamma$ process at the center of mass of $\sqrt{s} = 10.58$ GeV by the *BABAR* Collaboration [20]:

$$s|F_{\eta\gamma}| = (0.229 \pm 0.031)\ \text{GeV},$$
$$s|F_{\eta'\gamma}| = 0.251 \pm 0.021)\ \text{GeV}. \tag{31}$$

In our LFQM calculation for the perturbative region, we find slightly different values for the timelike and

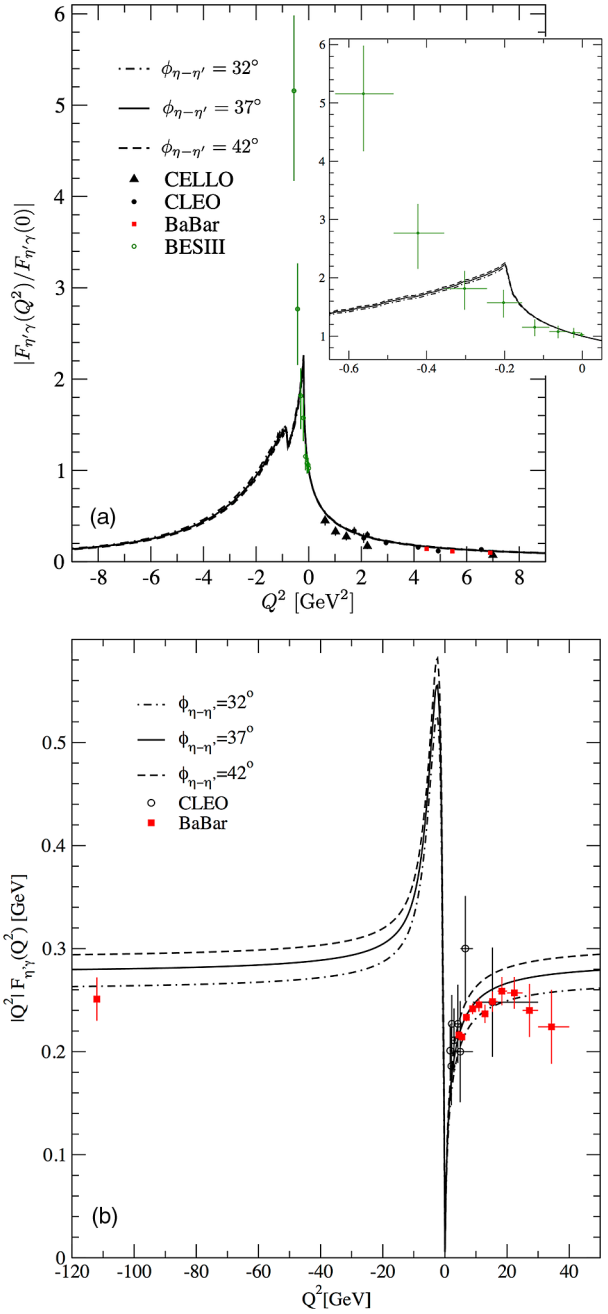

FIG. 7. (a) The normalized $\eta' \to \gamma^*\gamma$ transition form factor $|F_{\eta'\gamma}(Q^2)/F_{\eta'\gamma}(0)|$, and (b) $|Q^2F_{\eta'\gamma}(Q^2)|$ for both timelike ($q^2 = -Q^2 > 0$) and spacelike ($q^2 = -Q^2 < 0$) momentum transfer region. The same line codes are used as in Fig. 6 and the data are taken from [6,7,14,20].

spacelike η and η' TFFs, e.g. while the absolute spacelike values at $Q^2 = 112\,\mathrm{GeV}^2$ are $|Q^2F_{\eta(\eta')\gamma}(Q^2)| \simeq 0.191^{+0.024}_{-0.025}(0.284^{-0.017}_{+0.016})\,\mathrm{GeV}$, the timelike value at $q^2 = 112\mathrm{GeV}^2$ are $|q^2F_{\eta(\eta')\gamma}(q^2)| \simeq 0.178^{+0.024}_{-0.025}(0.280^{-0.017}_{+0.016})\,\mathrm{GeV}$ for $\phi = 37^{-5°}_{+5°}$, respectively. But the corresponding ratios of the spacelike to timelike η and η' TFFs at $|Q^2| = 112\ \mathrm{GeV}^2$ are about 1.07 and 1.02, respectively, regardless of the mixing angles. Our results at the timelike $q^2 = 112\ \mathrm{GeV}^2$ are also consistent with the perturbative QCD predictions [28], where $|q^2F_{\eta\gamma}(q^2)| \simeq 0.17\,\mathrm{GeV}$ and $|q^2F_{\eta'\gamma}(q^2)| \simeq 0.28\,\mathrm{GeV}$ were obtained. As stated in [51], while the *BABAR* result for $q^2F_{\eta\gamma}(q^2)$ at $q^2 = 112\ \mathrm{GeV}^2$ is about 2σ larger than the asymptotic prediction, the corresponding result for $q^2F_{\eta'\gamma}(q^2)$ from the *BABAR* Collaboration is in agreement with the asymptotic expectation. Thus, it is hard to estimate the correct $\eta - \eta'$ mixing angle with these two experimental data points at $q^2 = 112\ \mathrm{GeV}^2$ in the present time. More experimental data in perturbative region may be necessary to draw any definite conclusion on the mixing angle.

V. SUMMARY AND DISCUSSION

In this work, we investigated the $(\pi^0, \eta, \eta') \to \gamma^*\gamma$ transitions for the entire kinematic regions analyzing both spacelike and timelike TFFs in the standard LF (SLF) approach within the phenomenologically accessible realistic LFQM [58,59,61,62]. Performing the LF calculation in the covariant BS model as the first illustration, we used three different reference frames, i.e. (1) $q^+ \neq 0$ frame with $P^- = q^-$ and $\alpha = q^+/P^+ = q^2/M^2$, (2) $q^+ \neq 0$ frame with $P^+ = q^+$ (i.e., $\alpha = 1$), and (3) $q^+ = 0$ frame with $q^2 = -\mathbf{q}_\perp^2 = -Q^2$ (i.e, $\alpha = 0$), and found that all three different reference LF frames give exactly the same results to the one obtained from the manifestly covariant calculation as they must be. Especially, the calculation of $F_{P\gamma}$ using the $q^+ \neq 0$ frame with $\alpha = 1$ is found to be most effective for the analysis of the timelike region due to the absence of mixing between the internal transverse momentum and the external virtual photon momentum that leads to the very simple pole structure $1/(q^2 - M_0^2)$ in the form factor. We also confirmed the absence of the LF zero mode in pseudoscalar meson TFFs. As a consequence, the $q^+ = 0$ frame (i.e. $\alpha = 0$) calculation exhibits that the meson TFF using the plus component of the current is immune to the zero mode. Thus, in the $q^+ = 0$ frame (i.e., the well-known Drell-Yan-West frame), the complete total amplitude is provided by just the valence contribution depicted in Fig. 1(b). As a consistency check for our numerical calculations, we also compared our direct results of the form factor $F(q^2) = \mathrm{Re}F(q^2) + i\mathrm{Im}F(q^2)$ with those obtained from the dispersion relations (DR) and found the excellent agreement between the two results. This assured the reliability of our numerical calculation in the timelike region.

We then mapped this exactly solvable manifestly covariant BS model to the standard LFQM following the same correspondence relation Eq. (15) between the two models that we found in our previous analysis of two-point and three-point functions for the pseudoscalar and vector mesons [69,70]. This allowed us to apply the more phenomenologically accessible Gaussian wave function provided by the LFQM analysis of meson mass spectra [58,59,61,62]. In the analysis of the meson-photon TFFs

using our LFQM, we took the $q^+ \neq 0$ frame with $\alpha = 1$ which is the most convenient frame to analyze the timelike region compare to any other reference frames. For the $(\eta, \eta') \to \gamma^*\gamma$ transitions, we used the $\eta - \eta'$ mixing angle ϕ in the quark-flavor basis varying the ϕ values in the range of $\phi = 37^{+5^\circ}_{-5}$ to check the sensitivity of our LFQM. For the numerical analyses of the $P \to \gamma^*\gamma(P = \pi^0, \eta, \eta')$ TFFs using our LFQM, we investigated both the low-energy and high-energy regimes.

For the low-energy regime, our results for the TFFs and their slope parameters are in good agreement with the available data from the Dalitz decays of (π^0, η, η') mesons. Especially, in the low momentum transfer region, the η and η' TFFs are rather insensitive to the mixing angles. For the analysis of timelike form factor near resonance region, the maximum value of $F_{\pi\gamma}$ occurs at $q^2(=-Q^2) \simeq 4m_Q^2$ due to the virtual photon wave function term $1/(M_0^2 - q^2)$ in Eq. (20). The ρ-pole type resonance may be achieved by finding more realistic form of the photon wave function, which is open for the future work. For the resonance properties of $F_{\eta\gamma}$ and $F_{\eta'\gamma}$, the primary and secondary peaks of both $F_{\eta\gamma}$ and $F_{\eta'\gamma}$ occurs at $q^2 \simeq 4m_Q^2(Q = u, d)$ and $q^2 \simeq 4m_s^2$, respectively, regardless of their mixing angles. We also anticipate from our LFQM analysis that the experimental data for both timelike $F_{\eta\gamma}$ and $F_{\eta'\gamma}$ would show peaks near $q^2 = M_\rho^2$ (primary) and $q^2 = M_\phi^2$ (secondary) corresponding to our primary and secondary peaks at $q^2 = 4m_{u(d)}^2$ and m_s^2, respectively.

For the high-energy regime, our result of $|Q^2 F_{P\gamma}(Q^2)|$ does not show any steep rising behavior for high $|Q^2|$ region as measured from the *BABAR* Collaboration [18] but shows scaling behavior for high $|Q^2|$ consistent with the perturbative QCD prediction. This is ascribed to the fact that our twist-2 DA [59,70] is highly suppressed at the endpoints ($x = 0, 1$) unlike the flat DA [22,23] showing the enhancement at the endpoints. Especially, in our LFQM calculation for the perturbative region, we find slightly different values for the timelike and spacelike TFFs, e.g., the ratios of the spacelike to timelike TFFs at $|Q^2| = 112$ GeV^2 are about 1.04 for π^0 TFF and 1.07 (1.02) for $\eta(\eta')$, regardless of the $\eta - \eta'$ mixing angles. While the *BABAR* result [20] for $|q^2 F_{\eta\gamma}(q^2)|$ at $q^2 = 112$ GeV^2 is about 2σ larger than the asymptotic prediction, the corresponding result for $|q^2 F_{\eta'\gamma}(q^2)|$ from the *BABAR* Collaboration is in agreement with the asymptotic expectation. Thus, it is hard to predict the correct $\eta - \eta'$ mixing angle with these two experimental data points at $q^2 = 112$ GeV^2 at present time. More experimental data in perturbative region may be necessary to draw any definite conclusion on the mixing angle.

While the pseudoscalar meson vertex $\Gamma_P = \gamma_5$ is taken in this work, the generalization of the vertex including the axial vector coupling [102] may be considered for further study. The work along this direction is underway.

ACKNOWLEDGMENTS

H.-M. Choi was supported by the National Research Foundation of Korea (NRF) (Grant No. NRF-2017R1D1A1B03033129). H.-Y. Ryu was supported by the NRF grant funded by the Korea government(MSIP) (No. 2015R1A2A2A01004238). C.-R. Ji was supported in part by the US Department of Energy (Grant No. DE-FG02-03ER41260).

APPENDIX: $\eta - \eta'$ MIXING

In this appendix, we provide the comparison of the $\eta - \eta'$ mixing angle between the octet-singlet basis and quark-flavor basis. The octet-singlet mixing angle θ of η and η' is known to be in the range of -10° to -23° [87]. The physical η and η' are the mixtures of the flavor $SU(3)$ octet η_8 and singlet η_0 states:

$$\begin{pmatrix} \eta \\ \eta' \end{pmatrix} = \begin{pmatrix} \cos\theta & -\sin\theta \\ \sin\theta & \cos\theta \end{pmatrix} \begin{pmatrix} \eta_8 \\ \eta_0 \end{pmatrix}, \tag{A1}$$

where $\eta_8 = (u\bar{u} + d\bar{d} - 2s\bar{s})/\sqrt{6}$ and $\eta_0 = (u\bar{u} + d\bar{d} + s\bar{s})/\sqrt{3}$. Analogously, in terms of the quark-flavor(QF) basis $\eta_q = (u\bar{u} + d\bar{d})/\sqrt{2}$ and $\eta_s = s\bar{s}$, one obtains [72]

$$\begin{pmatrix} \eta \\ \eta' \end{pmatrix} = \begin{pmatrix} \cos\phi & -\sin\phi \\ \sin\phi & \cos\phi \end{pmatrix} \begin{pmatrix} \eta_q \\ \eta_s \end{pmatrix}. \tag{A2}$$

The two schemes are equivalent to each other by $\phi = \theta + \arctan\sqrt{2}$ when $\mathrm{SU}_f(3)$ symmetry is perfect. Although it was frequently assumed that the decay constants follow the same pattern of state mixing, the mixing properties of the decay constants will generally be different from those of the meson state since the decay constants only probe the short-distance properties of the valence Fock states while the state mixing refers to the mixing of the overall wave function [72].

Defining $\langle P(p)|J_{\mu 5}^{q(s)}|0\rangle = -if_P^{q(s)} p^\mu$ $(P = \eta, \eta')$ in the QF basis, the four parameters f_P^q and f_P^s can be expressed in terms of two mixing angles (ϕ_q and ϕ_s) and two decay constants (f_q and f_s), i.e., [72],

$$\begin{pmatrix} f_\eta^q & f_\eta^s \\ f_{\eta'}^q & f_{\eta'}^s \end{pmatrix} = \begin{pmatrix} \cos\phi_q & -\sin\phi_s \\ \sin\phi_q & \cos\phi_s \end{pmatrix} \begin{pmatrix} f_q 0 \\ 0 f_s \end{pmatrix}. \tag{A3}$$

The difference between the mixing angles $\phi_q - \phi_s$ is due to the Okubo-Zweig-Iizuka(OZI)-violating effects [73] and is found to be small ($\phi_q - \phi_s < 5^\circ$). The OZI rule implies that the difference between ϕ_q and ϕ_s vanishes (i.e., $\phi_q = \phi_s = \phi$) to leading order in the $1/N_c$ expansion. Similarly, the four parameters f_P^8 and f_P^0 in the octet-singlet basis may be written in terms of two angles (θ_8 and θ_0) and two decay constants (f_8 and f_0). However, in this case, θ_8 and θ_0 turn out to differ considerably and become equal only in the $\mathrm{SU}_f(3)$ symmetry limit [72,74].

[1] E. Czerwinski, S. Eidelman, C. Hanhart, B. Kubis, A. Kupść, S. Leupold, P. Moskal, and S. Schadmand, arXiv:1207.6556.
[2] T. Husek and S. Leupold, Eur. Phys. J. C **75**, 586 (2015).
[3] F. Jegerlehner and A. Nyffeler, Phys. Rep. **477**, 1 (2009).
[4] A. Nyffeler, Phys. Rev. D **94**, 053006 (2016).
[5] A. Gérardin, H. Meyer, and A. Nyffeler, Phys. Rev. D **94**, 074507 (2016).
[6] H.-J. Behrend *et al.* (CELLO Collaboration), Z. Phys. C **49**, 401 (1991).
[7] J. Gronberg *et al.* (CLEO Collaboration), Phys. Rev. D **57**, 33 (1998).
[8] A. Denig (BESIII Collaboration), Nucl. Part. Phys. Proc. **260**, 79 (2015).
[9] R. Arnaldi *et al.* (NA60 Collaboration), Phys. Lett. B **677**, 260 (2009).
[10] C. Lazzeroni *et al.* (NA62 Collaboration), Phys. Lett. B **768**, 38 (2017).
[11] P. Aguar-Bartomomé *et al.* (A2 Collaboration), Phys. Rev. C **89**, 044608 (2014).
[12] H. Berghäuser *et al.* (A2 Collabotation), Phys. Lett. B **701**, 562 (2011).
[13] P. Adlarson *et al.* (A2 Collaboration), Phys. Rev. C **95**, 025202 (2017).
[14] M. Ablikim *et al.* (BESIII Collaboration), Phys. Rev. D **92**, 012001 (2015).
[15] G. P. Lepage and S. J. Brodsky, Phys. Rev. D **22**, 2157 (1980).
[16] A. V. Efremov and A. V. Radyushkin, Phys. Lett. **94B**, 245 (1980).
[17] V. L. Chernyak and A. R. Zhitnitsky, Phys. Rep. **112**, 173 (1984).
[18] B. Aubert *et al.* (*BABAR* Collaboration), Phys. Rev. D **80**, 052002 (2009).
[19] S. Uehara *et al.* (Belle Collaboration), Phys. Rev. D **86**, 092007 (2012).
[20] P. del Amo Sanchez *et al.* (*BABAR* Collaboration), Phys. Rev. D **84**, 052001 (2011).
[21] S. V. Mikhaillov and N. G. Stefanis, Nucl. Phys. **B821**, 291 (2009).
[22] A. V. Radyushkin, Phys. Rev. D **80**, 094009 (2009).
[23] M. V. Polyakov, JETP Lett. **90**, 228 (2009).
[24] E. R. Arriola and W. Broniowski, Phys. Rev. D **67**, 074021 (2003).
[25] A. E. Dorokhov, Phys. Part. Nucl. Lett. **7**, 229 (2010).
[26] A. E. Dorokhov and E. A. Kuraev, Phys. Rev. D **88**, 014038 (2013).
[27] X.-G. Wu and T. Huang, Phys. Rev. D **82**, 034024 (2010).
[28] P. Kroll, Eur. Phys. J. C **71**, 1623 (2011).
[29] S. S. Agaev, V. M. Braun, N. Offen, and F. A. Porkert, Phys. Rev. D **83**, 054020 (2011); **86**, 077504 (2012).
[30] H. L. L. Roberts, C. D. Roberts, A. Bashir, L. X. Gutiérrez-Guerrero, and P. C. Tandy, Phys. Rev. C **82**, 065202 (2010).
[31] K. Raya, L. Chang, A. Bashir, J. Javier Cobos-Martinez, L. Xiomara Gutiérrez-Guerrero, C. D. Roberts, and P. C. Tandy, Phys. Rev. D **93**, 074017 (2016).
[32] S. J. Brodsky, F.-G. Cao, and Guy F. de Téramond, Phys. Rev. D **84**, 033001 (2011); **84**, 075012 (2011).
[33] A. P. Bakulev, S. V. Mikhaillov, A. V. Pimikov, and N. G. Stefanis, Phys. Rev. D **86**, 031501(R) (2012).
[34] N. G. Stefanis, A. P. Bakulev, S. V. Mikhaillov, and A. V. Pimikov, Phys. Rev. D **87**, 094025 (2013).
[35] W. Lucha and D. Melikhov, J. Phys. G **39**, 045003 (2012); Phys. Rev. D **86**, 016001 (2012).
[36] I. Balakireva, W. Lucha, and D. Melikhov, Phys. Rev. D **85**, 036006 (2012).
[37] N. G. Stefanis, W. Schroers, and H.-Ch. Kim, Eur. Phys. J. C **18**, 137 (2000).
[38] N. Kochelev and V. Vento, Phys. Rev. D **81**, 034009 (2010).
[39] H. N. Li, Y. L. Shen, and Y. M. Wang, J. High Energy Phys. 01 (2014) 004.
[40] C.-W. Hwang, Phys. Rev. D **64**, 034011 (2001).
[41] C.-C. Lih and C.-Q. Geng, Phys. Rev. C **85**, 018201 (2012).
[42] B. El-Bennich, J. P. B. C. de Melo, and T. Frederico, Few Body Syst. **54**, 1851 (2013).
[43] J. P. B. C. de Melo, B. El-Bennich, and T. Frederico, Few Body Syst. **55**, 373 (2014).
[44] D. Gómez Dumm, S. Noguera, N. N. Scoccola, and S. Scopetta, Phys. Rev. D **89**, 054031 (2014).
[45] S. Noguera and S. Scopetta, Eur. Phys. J. A **46**, 197 (2010); **48**, 143 (2012).
[46] T. Feldmann and P. Kroll, Eur. Phys. J. C **5**, 327 (1998).
[47] A. E. Dorokhov, A. E. Radzhabov, and A. S. Zhevlakov, Eur. Phys. J. C **71**, 1702 (2011).
[48] S. S. Agaev and N. G. Stefanis, Phys. Rev. D **70**, 054020 (2004).
[49] S. S. Agaev, V. M. Braun, N. Offen, F. A. Porkert, and A. Schäfer, Phys. Rev. D **90**, 074019 (2014).
[50] R. Escribano, P. Masjuan, and P. Sanchez-Puetas, Phys. Rev. D **89**, 034014 (2014).
[51] P. Kroll and K. Passek-Kumerički, J. Phys. G **40**, 075005 (2013); Phys. Rev. D **67**, 054017 (2003).
[52] D. Melikhov and B. Stech, Phys. Lett. B **718**, 488 (2012).
[53] Y.-M. Wang and Y.-L. Shen, arXiv:1706.05680.
[54] B. Aubert *et al.* (*BABAR* Collaboration), Phys. Rev. D **74**, 012002 (2006).
[55] A. P. Bakulev, A. V. Radyushkin, and N. G. Stefanis, Phys. Rev. D **62**, 113001 (2000).
[56] R. Escribano, P. Masjuan, and P. Sanchez-Puetas, Eur. Phys. J. C **75**, 414 (2015).
[57] R. Escribano, S. González-Solís, P. Masjuan, and P. Sanchez-Puetas, Phys. Rev. D **94**, 054033 (2016).
[58] H.-M. Choi and C.-R. Ji, Phys. Rev. D **59**, 074015 (1999).
[59] H.-M. Choi and C.-R. Ji, Phys. Rev. D **75**, 034019 (2007).
[60] H.-M. Choi and C.-R. Ji, Few Body Syst. **57**, 497 (2016).
[61] H.-M. Choi and C.-R. Ji, Phys. Lett. B **460**, 461 (1999).
[62] H.-M. Choi and C.-R. Ji, Phys. Rev. D **80**, 054016 (2009).
[63] M. Burkardt, Phys. Rev. D **47**, 4628 (1993).
[64] S. J. Brodsky and D. S. Hwang, Nucl. Phys. **B543**, 239 (1999).
[65] J. P. B. C. de Melo, J. H. O. Sales, T. Frederico, and P. U. Sauer, Nucl. Phys. **A631**, 574c (1998).
[66] H.-M. Choi and C.-R. Ji, Phys. Rev. D **58**, 071901(R) (1998).
[67] B. L. G. Bakker, H.-M. Choi, and C.-R. Ji, Phys. Rev. D **65**, 116001 (2002).
[68] B. L. G. Bakker, H.-M. Choi, and C.-R. Ji, Phys. Rev. D **67**, 113007 (2003).

[69] H.-M. Choi and C.-R. Ji, Phys. Rev. D **89**, 033011 (2014).
[70] H.-M. Choi and C.-R. Ji, Phys. Rev. D **91**, 014018 (2015).
[71] H.-M. Choi and C.-R. Ji, Phys. Rev. D **95**, 056002 (2017); Few Body Syst. **58**, 31 (2017).
[72] T. Feldmann, P. Kroll, and B. Stech, Phys. Rev. D **58**, 114006 (1998); Phys. Lett. B **449**, 339 (1999).
[73] T. Feldmann, Int. J. Mod. Phys. A **15**, 159 (2000).
[74] H. Leutwyler, Nucl. Phys. B (Proc. Suppl.) **64**, 223 (1998).
[75] J. Schechter, A. Subbaraman, and H. Weigel, Phys. Rev. D **48**, 339 (1993).
[76] W. Jaus, Phys. Rev. D **44**, 2851 (1991).
[77] W. Jaus, Phys. Rev. D **41**, 3394 (1990).
[78] P. L. Chung, F. Coester, and W. N. Polyzou, Phys. Lett. B **205**, 545 (1988).
[79] H.-M. Choi, Phys. Rev. D **75**, 073016 (2007).
[80] H. J. Melosh, Phys. Rev. D **9**, 1095 (1974); P. L. Chung, F. Coester, B. D. Keister, and W. N. Polyzou, Phys. Rev. C **37**, 2000 (1988).
[81] A. V. Radyushkin, Phys. Lett. B **735**, 417 (2014).
[82] S. L. Adler, Phys. Rev. **177**, 2426 (1969).
[83] J. S. Bell and R. Jackiw, Nuovo Cimento A **60**, 47 (1969).
[84] F. Ambrosino *et al.* (KLOE Collaboration) Phys. Lett. B **648**, 267 (2007).
[85] N. H. Christ, C. Dawson, T. Izubuchi, C. Jung, Q. Liu, R. D. Mawhinney, C. T. Sachrajda, A. Soni, and R. Zhou, Phys. Rev. Lett. **105**, 241601 (2010).
[86] J. F. Donoghue, B. R. Holstein, and Y. C. R. Lin, Phys. Rev. Lett. **55**, 2766 (1985).
[87] C. Patrignani *et al.* (Particle Data Group), Chin. Phys. C **40**, 100001 (2016).
[88] D. Babusci *et al.* (KLOE-2 Collaboration), J. High Energy Phys. 01 (2013) 119.
[89] J. Botts and G. Sterman, Nucl. Phys. **B325**, 62 (1989).
[90] H. n. Li and G. Sterman, Nucl. Phys. **B381**, 129 (1992).
[91] H. Fonvieille *et al.*, Phys. Lett. B **233**, 65 (1989).
[92] F. Farzanpay *et al.*, Phys. Lett. B **278**, 413 (1992).
[93] R. Meijer Drees *et al.*, Phys. Rev. D **45**, 1439 (1992).
[94] P. Masjuan, Phys. Rev. D **86**, 094021 (2012).
[95] E. R. Arriola and W. Broniowski, Phys. Rev. D **81**, 094021 (2010).
[96] J. Bijnens, A. Bramon, and F. Cornet, Z. Phys. C **46**, 599 (1990).
[97] K. Kampf, M. Knecht, and J. Novotny, Eur. Phys. J. C **46**, 191 (2006).
[98] H. R. Grigoryan and A. V. Radyushkin, Phys. Rev. D **77**, 115024 (2008).
[99] H. R. Grigoryan and A. V. Radyushkin, Phys. Rev. D **78**, 115008 (2008); S. K. Domokos, H. R. Grigoryan, and J. A. Harvey, Phys. Rev. D **80**, 115018 (2009).
[100] P. Colangelo, F. De Fazio, J. J. Sanz-Cillero, F. Giannuzzi, and S. Nicotri, Phys. Rev. D **85**, 035013 (2012).
[101] R. I. Dzhelyadin *et al.* (Lepton-G Collaboration), Phys. Lett. **88B**, 379 (1979); JETP Lett. **30**, 359 (1979).
[102] T. N. Pham and X. Y. Pham, Int. J. Mod. Phys. A **26**, 4125 (2011).